



## ENGINEERING

# Highly stretchable and customizable microneedle electrode arrays for intramuscular electromyography

**Qinai Zhao<sup>1,2</sup>, Ekaterina Gribkova<sup>3,4</sup>, Yiyang Shen<sup>2,5</sup>, Jilai Cui<sup>3,4</sup>, Noel Naughton<sup>6,7</sup>, Liangshu Liu<sup>1,2</sup>, Jaemin Seo<sup>1,2</sup>, Baixin Tong<sup>2,5</sup>, Mattia Gazzola<sup>6,8,9</sup>, Rhanor Gillette<sup>3,10</sup>, Hangbo Zhao<sup>1,2,11\*</sup>**

Stretchable three-dimensional (3D) penetrating microelectrode arrays have potential utility in various fields, including neuroscience, tissue engineering, and wearable bioelectronics. These 3D microelectrode arrays can penetrate and conform to dynamically deforming tissues, thereby facilitating targeted sensing and stimulation of interior regions in a minimally invasive manner. However, fabricating custom stretchable 3D microelectrode arrays presents material integration and patterning challenges. In this study, we present the design, fabrication, and applications of stretchable microneedle electrode arrays (SMNEAs) for sensing local intramuscular electromyography signals ex vivo. We use a unique hybrid fabrication scheme based on laser micromachining, micro-fabrication, and transfer printing to enable scalable fabrication of individually addressable SMNEA with high device stretchability (60 to 90%). The electrode geometries and recording regions, impedance, array layout, and length distribution are highly customizable. We demonstrate the use of SMNEAs as bioelectronic interfaces in recording intramuscular electromyography from various muscle groups in the buccal mass of *Aplysia*.

Copyright © 2024, the  
Authors, some rights  
reserved; exclusive  
licensee American  
Association for the  
Advancement of  
Science. No claim to  
original U.S.  
Government Works.  
Distributed under a  
Creative Commons  
Attribution  
NonCommercial  
License 4.0 (CC BY-NC).

## INTRODUCTION

Microelectrode arrays (MEAs) have been a widely used technological platform for biomedical applications including electrophysiological recording (1, 2), electrochemical sensing (3, 4), and electrical stimulation (5, 6). Conventional MEAs have planar electrode layouts fabricated on rigid substrates (e.g., silicon or glass) using lithography-based processes, such as one-dimensional (1D) Michigan probes for neural recording (7) and 2D MEAs on glass for cellular or tissue-level analysis (8, 9). Out-of-plane 2D MEAs such as the Utah array (10) expand the electrode-bio interface to the third dimension. Moreover, MEAs that allow electrode coverage in 3D space are achievable by stacking 1D or 2D MEAs (11, 12), 3D printing (13), or complex nanofabrication techniques such as focused ion beam (FIB) milling (14). 3D MEAs can penetrate surface layers of tissues, thereby allowing probing of physiological signals and electrical stimulation of interior regions in a minimally invasive manner. Such multichannel, deep-tissue sensing and stimulation capabilities can provide valuable information and control over a wide range of 3D biological systems such as skin dermis layers (15); neural (16), neuromuscular (17), and skeletal tissues (18); or organoids (19).

In addition to achieving high electrode density in 3D space, advances in flexible or stretchable MEAs can mitigate the mechanical mismatch between rigid MEAs and soft, curvilinear, and dynamic

biological tissues. Flexible 3D MEAs are attainable by fabricating rigid 3D electrodes and associated electrical interconnects directly on, or via a transfer process to, flexible polymeric substrates, including thinning of silicon (20), replica molding (21, 22), magnetorheological drawing (23), or via controlled bending of 2D MEAs (24, 25). While flexible 3D MEAs provide improved conformability to irregular or curvilinear surfaces, the stretchability of these devices is highly desirable as it enables the electrodes to follow tissue deformations such as in the myocardium of the human heart [approximately –15 to –25% longitudinal strain during contraction (26)], skeletal muscles [up to 30 to 40% radial expansion (27)], or human skin [up to 70% strain (28)]. Dynamic conformability of 3D MEAs can favor stable bioelectronic interfacing, leading to enhanced recording signal quality and reduced tissue damage, all of which are critical for ex vivo or in vivo applications. However, stretchable 3D MEAs present substantial fabrication challenges, mainly due to the incompatibility of existing rigid, penetrating electrode fabrication processes and the stretchability requirements of the accompanying constituent materials and structures. Minimally invasive penetration requires thin electrodes, typically in the form of microneedles. To enable penetration of relatively long and thin microneedles into tissues without mechanical buckling or fracture, high-modulus materials are needed, such as silicon, glass, and metals. Existing stretchable 3D MEAs include stainless steel microneedle electrode arrays (40% stretchability) assembled manually on a silicone substrate (17) and silicon-based microneedle electrodes fabricated by complex etching with approximately 20 to 45% maximum stretchability (29, 30). However, these solutions are limited in terms of attainable stretchability, scalability, and cost. In addition, customization of electrode geometry and active recording and stimulation regions remain a challenge.

Here, we present design, fabrication, and electrophysiological sensing applications of stretchable microneedle electrode array (SMNEA) devices. A low-cost and scalable microneedle electrode fabrication process combining laser micromachining, replica molding, microfabrication, and transfer printing allows the formation of individually addressable, high-modulus microneedle arrays connected

<sup>1</sup>Department of Aerospace and Mechanical Engineering, University of Southern California, Los Angeles, CA, USA. <sup>2</sup>Center for Advanced Manufacturing, University of Southern California, Los Angeles, CA, USA. <sup>3</sup>Neuroscience Program, University of Illinois at Urbana-Champaign, Urbana, IL, USA. <sup>4</sup>Coordinated Science Laboratory, University of Illinois at Urbana-Champaign, Urbana, IL, USA. <sup>5</sup>Mork Family Department of Chemical Engineering and Materials Science, University of Southern California, Los Angeles, CA, USA. <sup>6</sup>Department of Mechanical Science and Engineering, University of Illinois at Urbana-Champaign, Urbana, IL, USA. <sup>7</sup>Beckman Institute for Advanced Science and Technology, University of Illinois at Urbana-Champaign, Urbana, IL, USA. <sup>8</sup>National Center for Supercomputing Applications, University of Illinois at Urbana-Champaign, Urbana, IL, USA. <sup>9</sup>Carl R. Woese Institute for Genomic Biology, University of Illinois at Urbana-Champaign, Urbana, IL, USA. <sup>10</sup>Department of Molecular and Integrative Physiology, University of Illinois at Urbana-Champaign, Urbana, IL, USA. <sup>11</sup>Alfred E. Mann Department of Biomedical Engineering, University of Southern California, Los Angeles, CA, USA.

\*Corresponding author. Email: hangbozh@usc.edu

to serpentine-shaped interconnects. Covalent bonding of the micro-needles and interconnects to an elastomeric substrate yields high stretchability. Metallization and a gel-based chemical etching technique applied to the microneedles yield microneedle electrode arrays with controllable exposed areas. The fabrication scheme uniquely combines scalability with varying electrode lengths, controlled recording regions and electrode impedance, device stretchability of 60 to 90%, and relatively large electrode modulus ( $E = 6.6$  GPa). Measurements of intramuscular electromyography (EMG) in the buccal mass of *Aplysia* and comparisons with results of surface EMG demonstrate the utility of these stretchable penetrating MEAs in the context of dynamic 3D tissues.

## RESULTS

### Stretchable microneedle electrode array

The basic structure of the SMNEAs consists of arrays of microneedle electrodes individually connected by serpentine interconnects. Both microneedles and interconnects are covalently bonded to a silicone elastomer (Ecoflex 00-30). The microneedles, conical in shape, are made of polyimide (PI; PI-2610) with a conductive coating of Cr/Au (10 nm/150 nm in thickness) and an insulating coating of parylene C (3  $\mu\text{m}$  in thickness). The serpentine interconnects are PI filaments (30  $\mu\text{m}$  in thickness and 70  $\mu\text{m}$  in width) with a thin film of Cr/Au. These conductive serpentine filaments provide electrical connections between individual microneedle electrodes and external electronics. Upon stretching of the elastomeric substrate, the serpentine interconnects bonded to the substrate can accommodate deformations through in-plane bending of the arc-shaped patterns (Fig. 1A) (31). The strong covalent bonding between the microneedles with the interconnects and the elastomeric substrate prevents delamination between them (fig. S1 and movie S1). Figure 1 (B and C) shows the fabricated SMNEA.

The fabrication of the SMNEA uses a hybrid approach combining laser micromachining, replica molding, microfabrication, and transfer printing. The process starts with the creation of conical cavities by laser ablation of polydimethylsiloxane (PDMS) using a low-cost CO<sub>2</sub> laser cutter (fig. S2A). The PDMS with cavities serves as a mold for replicating microneedle structures. Controlling the ablation pattern, laser power, and focus can yield conical cavities with various base diameters and depths and therefore the geometries of microneedles (figs. S2B and S3). The replica molding process starts with surface treatment of the PDMS mold using atmospheric plasma, followed by deposition of liquid PI-2610 precursor into the cavities, spin coating, and a multistep curing process (detailed steps appear in Materials and Methods). The result is an array of PI microneedles with desired geometries inside the PDMS cavities connected by a thin film (approximately 30  $\mu\text{m}$  in thickness) of PI on the top surface (fig. S4). Typical microneedles have base diameters ranging from 300 to 800  $\mu\text{m}$ , lengths ranging from 500 to 2000  $\mu\text{m}$ , and tip diameters of approximately 10 to 30  $\mu\text{m}$ .

As a result of spin coating, the PI thin film is flat, allowing the use of lithography-based microfabrication processes. Patterned etching of the PI thin film creates an outline (30  $\mu\text{m}$  in width) that defines the serpentine interconnects and the edges of the microneedle bases (fig. S5). Subsequent deposition of a Ti/SiO<sub>2</sub> layer on the PI surface allows covalent surface reactions between the SiO<sub>2</sub> and an oxygen plasma-treated silicone elastomer film (Ecoflex, approximately 200  $\mu\text{m}$  in thickness) (18, 32, 33), enabling the transfer of the

microneedle arrays from the PDMS mold to the silicone elastomer. Deposition of a thin Cr/Au layer metallizes the microneedles and serpentine filaments, followed by the removal of the excess PI film outside of the outlines. Figure 2 shows a schematic illustration of the fabrication process for the individually addressable SMNEA. This hybrid fabrication strategy allows the formation of highly customized microneedle geometries and array layouts using low-cost laser ablation and scalable microfabrication processes. Arrays of stretchable microneedle electrodes with controllable microneedle lengths can be created using this hybrid fabrication approach (Fig. 1, D to F). The layouts of the PI pattern and the sacrificial layer pattern for the SMNEA shown in Fig. 1 (B and E) appear in figs. S6 and S7.

### Control of electrical recording regions

Metallization of the PI microneedles and interconnects creates conductive pathways from the microneedle surfaces to external electronics. For sensing or stimulation applications, control of the active bioelectronic interfacing region is important to target the regions of interest. This is commonly realized by conformal coverage of a thin layer of insulation materials (e.g., parylene C) on the conductive microneedles except for the tips, where the conductive layer is selectively exposed as the electronic interface with the target. Various techniques have been used to selectively insulate microneedle electrodes, including a sacrificial coating followed by etch back (34–36), selective etching of the insulation coating by FIB (37) or through a shadow mask (14, 38), mechanical tearing of the insulation coating (39), insulation of the microneedle bases through gravity-driven flow (40, 41) or spin coating (42), and bulk silicon etching (43). These techniques either lack reliable, precise control of the exposed areas or require complicated fabrication processes. A common limitation is that almost none of these techniques is applicable to an array of microneedles with varying lengths, with the exception of FIB etching of the insulation film, which is a serial and time-consuming process. The stretchability requirement of the SMNEA adds additional challenges to selective insulation. To address these challenges, we develop an approach that provides precise control over the exposed electrical recording regions, regardless of the microneedle length. The process starts with a conformal coating of parylene C (3  $\mu\text{m}$  in thickness) on the microneedles and the Ecoflex substrate, followed by patterned deposition of a hard Cu mask (200 nm in thickness) through a shadow mask (Fig. 3A) that prevents Cu deposition outside of the microneedle surfaces. A key step in creating a well-defined recording area is the use of a gel etchant that can etch the Cu coating at the tips of the microneedles. The gel etchant is formed by soaking 0.6% agarose gel in a mixture of FeCl<sub>3</sub>/HCl solution to allow diffusion of FeCl<sub>3</sub>/HCl into the nanoporous gel. A brief (approximately 5 s) insertion of the tip of the Cu-coated microneedle in the gel etchant allows the dissolution of the Cu film on the tip (movie S2). Oxygen plasma etching removes the partially exposed parylene with the remaining Cu film acting as the etch mask, which is subsequently removed using liquid FeCl<sub>3</sub>/HCl. Scanning electron microscopy (SEM) images after selective Cu etching appear in fig. S8.

The length of the etched Cu at the tip is controlled by adjusting the insertion depth of the microneedle into the gel etchant, which is easily controllable by a motorized stage with optical imaging (Fig. 3B). With the Cu hard mask removed at the tip, an oxygen plasma etching of the parylene coating selectively exposes the Au layer (Fig. 3C). The use of a gel etchant instead of a liquid-phase

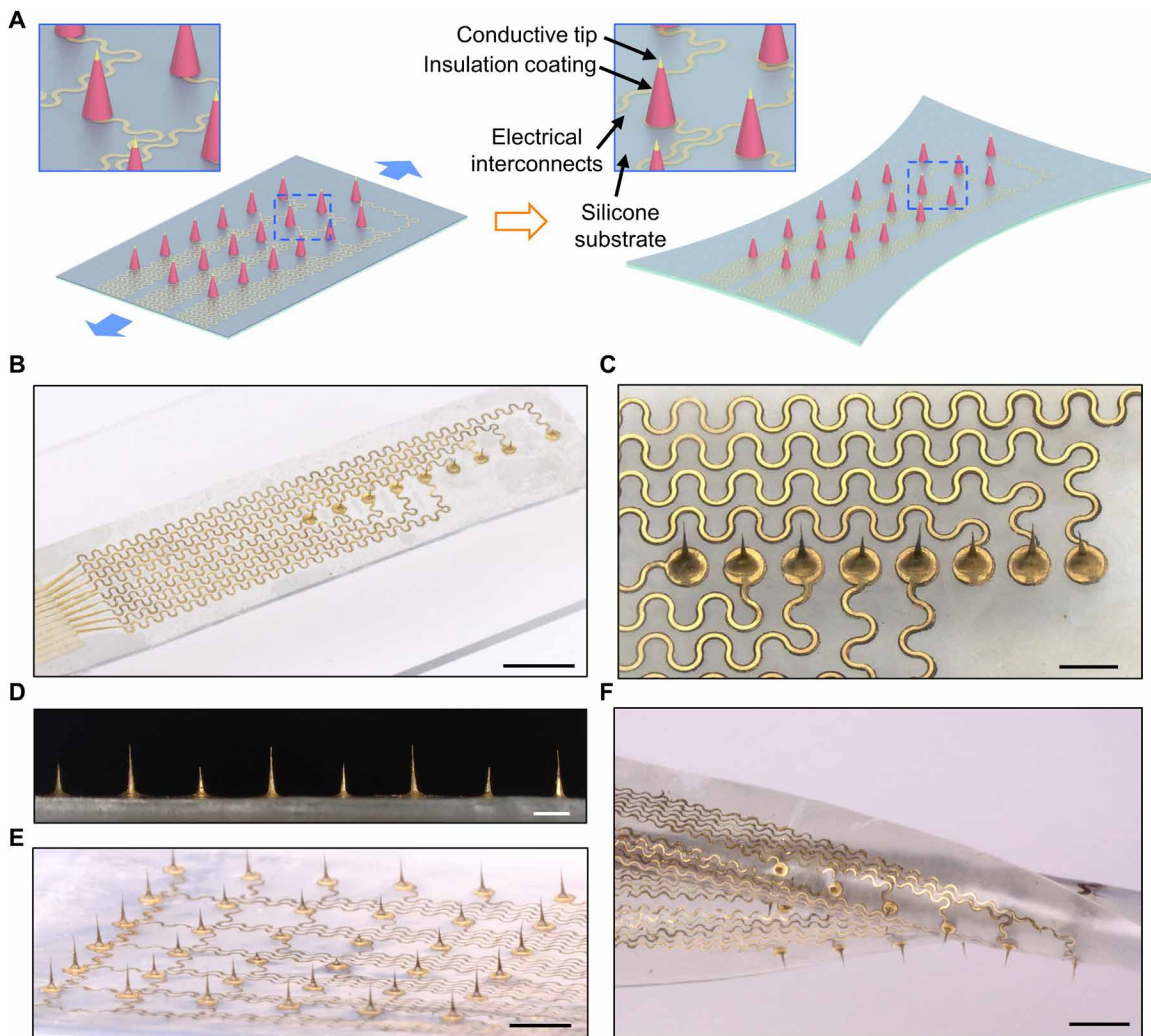


**Fig. 1. SMNEAs.** (A) Schematic illustration of an SMNEA device before and after uniaxial stretching. The SMNEA device consists of polymer microneedles with conductive and insulation coatings, electrical interconnects in serpentine layout, and a stretchable silicone substrate. (B and C) Optical images of an SMNEA device on a glass substrate at (B) low and (C) high magnification, showing the microneedle electrodes with serpentine interconnects. (D) Side-view optical image of an SMNEA with varying microneedle lengths, ranging from approximately 800 to 1500  $\mu\text{m}$ . (E) Angled-view optical image of a 6  $\times$  6 array of microneedle electrodes with varying lengths on a stretchable silicone substrate. (F) Optical image of a 6  $\times$  6 array of microneedle electrodes under stretching and twisting. Scale bars, 5 mm (B), 1 mm (C and D), and 3 mm (E and F).

$\text{FeCl}_3/\text{HCl}$  etchant minimizes the spreading of the liquid etchant along the microneedle surface due to liquid wetting on the Cu surface. The etchant spreading distance is approximately 20  $\mu\text{m}$  for a 5-to-10-s insertion into a gel etchant (fig. S9A) and increases only slightly for longer insertion times due to slower spreading speed. This contrasts with the complete spreading of etchant onto the microneedle within a few seconds when dipped in liquid-phase  $\text{FeCl}_3/\text{HCl}$  solution (movie S2). The relatively slow liquid etchant spreading on the Cu surface using the gel etchant is explained by the viscous drag of liquid through the nanoporous agarose gel (44). The measured lengths of the exposed tips are  $81.5 \pm 5.5 \mu\text{m}$  and  $141.5 \pm 6.5 \mu\text{m}$  for target lengths of 80  $\mu\text{m}$  (group I) and 140  $\mu\text{m}$  (group II), respectively (Fig. 3D). A unique feature of this gel-assisted etching method is its ability to control the tip exposure for microneedles of different lengths, which is readily achievable by shaping the gel etchants into narrow cubes into which individual

microneedles are inserted separately (fig. S9B). Controlled etching at the tips, for a large number of microneedles, is also possible with vision-based, automated insertion or by creating gel etchant patterns of predefined heights.

#### Characterization of electrical and mechanical properties of microneedle electrodes

The electrical impedance of the microneedle electrodes with exposed Au tips (approximately 80  $\mu\text{m}$  exposed length) appears in Fig. 3F. An additional coating of a nanoporous conductive layer on the exposed Au, such as platinum black (PtB), can decrease the electrical impedance of the microneedle electrode by increasing its surface area (19). Figure 3E shows an SEM image of a microneedle tip after the electrochemical deposition of a thin layer (approximately 1  $\mu\text{m}$  in thickness) of PtB coating, which effectively decreases the average electrode impedance measured in phosphate-buffered

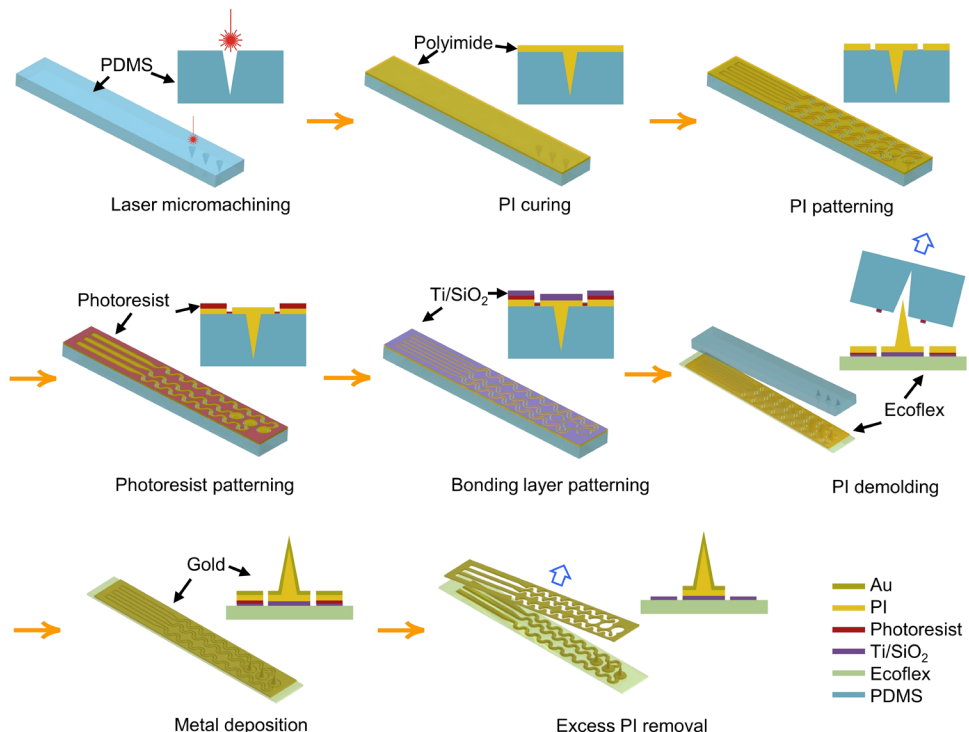


**Fig. 2. Schematic illustration of steps for fabricating SMNEAs.**

saline (PBS) from 66.2 to 1.6 kilohm at 1-kHz scanning frequency (Fig. 3F). The PtB coating reduces the electrode impedance without changing the microscale recording areas.

The core material of the microneedle is PI-2610, a thermosetting polymer with relatively high mechanical modulus and thermal resistance. A tensile test on a flat PI-2610 film (30  $\mu\text{m}$  in thickness; pattern appears in fig. S10A) prepared via a similar spin coating and curing process yields a stress-strain curve (fig. S10B). The PI-2610 film exhibits a linear stress-strain relation with a fitted Young's modulus of 6.63 GPa before fracturing at 1.76% tensile strain. This relatively high modulus compared to that of most other polymeric microneedles facilitates the insertion of the microneedles into target tissues without buckling or fracture.

Indentations of microneedles with similar geometries (approximately 920  $\mu\text{m}$  in length, 10 to 30  $\mu\text{m}$  in tip diameter) against flat rigid surfaces provide critical buckling loads. Figure S11A shows the force-displacement curves of the low Young's modulus PI (PI-2545,  $E = 2.3 \text{ GPa}$ ) microneedles and the high Young's modulus PI (PI-2610,  $E = 6.6 \text{ GPa}$ ) microneedles during indentation tests. The corresponding critical buckling loads appear in table S1A. The average critical buckling loads are 73 and 139 mN for PI-2545 and PI-2610 microneedles, respectively. The simulated critical buckling loads depend on the boundary conditions: The critical buckling load of a microneedle with a pinned tip is approximately 3.6 times greater than that with a free tip. The experimentally measured buckling loads for both PI-2545 and PI-2610 microneedles fall between the simulated values for free tip and pinned tip boundary conditions (fig. S11B). This is explained by the sliding of microneedle tips on the flat surface right before and during buckling (movie S3), which suggests an intermediate boundary condition between the free and pinned tip. For the same boundary condition, the critical buckling

load is linearly proportional to the Young's modulus of the microneedle (45). As a result, the critical buckling load of the PI-2610 microneedles is approximately three times higher than that of the PI-2545 microneedles.

Insertion tests of microneedles into PDMS (10:1 mixing ratio) provide additional comparison of microneedles with different moduli. The force-displacement curve during insertion (fig. S11C) yields the insertion force, defined as the load at the inflection point where penetration of the microneedle tips in the PDMS occurs. PI-2545 microneedles exhibit insertion forces in the range of 44 to 66 mN, close to their critical buckling loads from the indentation tests (67 to 80 mN). Subsequent increases in the resisting force after insertion lead to buckling and bending of the microneedles (movie S4 and table S1B). In contrast, the PI-2610 microneedles not only have larger critical buckling loads but also reduced insertion forces (25 to 30 mN) (fig. S11D). The lower insertion forces of PI-2610 microneedles as compared to those of PI-2545 microneedles, despite similar tip diameters, are explained by their smaller contact area (46), which likely stems from reduced tip bending due to the larger Young's modulus. As the critical buckling loads are approximately four to five times higher than the insertion forces, PI-2610 microneedles can be inserted into the PDMS without buckling.

The PI-2610 microneedles also exhibit robust mechanical and electrical properties over repeated insertions into soft materials. Au-coated microneedles exhibit no visible tip bending and slight (40%) increase in the electrical impedance after 1000 insertions into PDMS (20:1 mixing ratio; fig. S12 and movie S5). Similarly, PtB-coated microneedles show a 4.6% impedance increase without visible tip bending or PtB delamination after 1000 insertions into agarose gel (Fig. 3G, fig. S13, and movie S6).

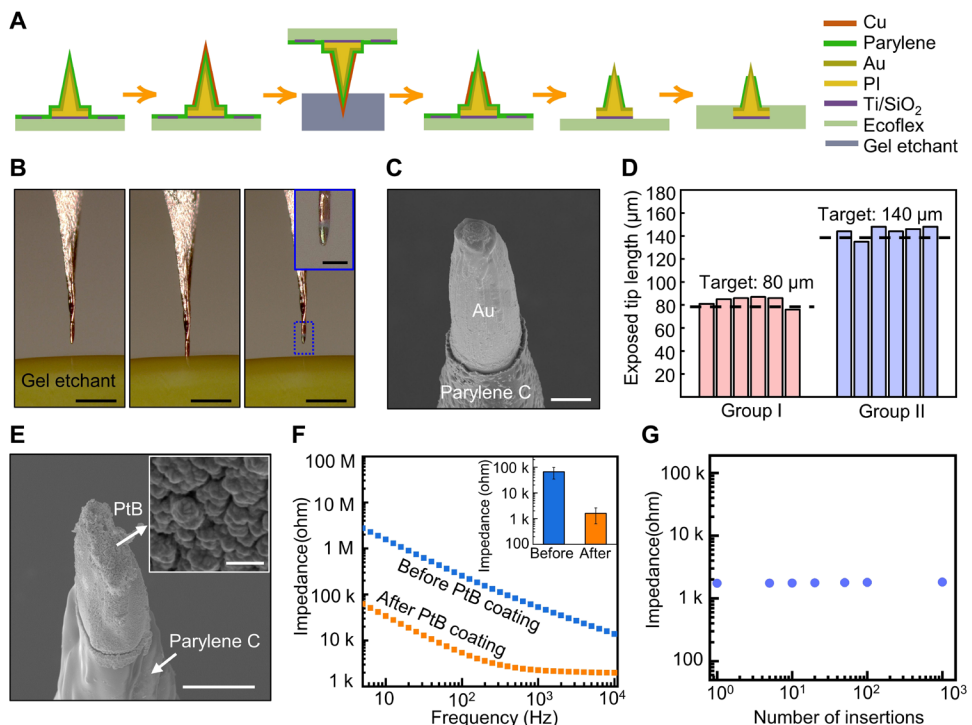


**Fig. 3. Control of the electrode recording region and electrical impedance.** (A) Schematic illustration of steps for fabricating a microneedle electrode with the conductive tip exposed. (B) Side-view microscopic images of gel-assisted etching of a copper hard mask at the tip of a microneedle. (C) SEM image of an Au-coated microneedle tip after selectively etching the parylene coating at the tip. (D) Statistics of exposed tip lengths from two groups of microneedles with target exposed tip lengths of 80 and 140  $\mu\text{m}$ , respectively. (E) SEM image of a microneedle tip after electrochemical deposition of PtB at the tip. (F) Electrode impedance spectra and average electrode impedance at 1-kHz scanning frequency before and after electrochemical deposition of PtB at the microneedle tip in 0.1 M phosphate-buffered saline (PBS). Error bars correspond to the calculated standard deviation from 12 electrode measurements. (G) Impedance of the electrode with PtB tip at 1 kHz under cyclic insertion into agarose gel. Scale bars, 200  $\mu\text{m}$  (B) (50  $\mu\text{m}$  in inset), 10  $\mu\text{m}$  (C), and 30  $\mu\text{m}$  (E) (1  $\mu\text{m}$  in inset).

Downloaded from https://www.science.org on May 01, 2024

### Mechanical stretchability of SMNEA

The microneedles and serpentine interconnects covalently bonded to the elastomeric substrate give rise to mechanical stretchability of the SMNEA. Figure 4A shows an SMNEA under stretching (66% tensile strain) and a combination of stretching (30% tensile strain) and twisting (180° rotation) deformations. Finite element analysis (FEA) provides quantitative strain distributions in the SMNEA constituent materials. For 66% stretching, the peak value of the maximum principal strain in the PI-2610 layer is observed near the serpentine edges, reaching 1.62%. For the combined stretching and twisting test, the peak value of the maximum principal strain in the PI is approximately 0.65%, located near the end of the serpentine interconnect region. The strain of the Au layer in these deformations is reported in fig. S14.

Uniaxial tensile testing of the SMNEA provides details on its stretchability limit. Figure 4B shows a series of side-view optical images of a representative SMNEA device with PtB coating at the tips under uniaxial stretching, with the device immersed in PBS for electrical impedance measurement (setup shown in fig. S15). Stretching of a single row of microneedle electrodes causes increased distances between them and straightening of the serpentine interconnects. The electrode impedance remains mostly unchanged below 40% strain, while significant increase in impedance appears from 60 to 90% strain (Fig. 4C). In this strain range, the maximum value of the maximum principal strain in the PI layer of the serpentine

interconnects approaches its fracture limit (1.76%, determined by tensile tests shown in fig. S10), breaking the serpentine interconnects (Fig. 4B). The strain in the Au layer remains within its fracture limit of 1 to 2% (47), suggesting that the stretchability is dictated by the PI layer. The measured variations in the stretchability of different electrodes likely originate from imperfections of the PI film fabrication and patterning as well as differences in local strain. The high stretchability and low tensile stiffness (~7 N/m below 60% strain) of the SMNEA allow it to follow the deformation of soft target materials with stable microneedle insertion and reduced mechanical stress applied to the target. Figure S16 and movie S7 show an example of SMNEA inserted in PDMS under cyclic stretching. The 60 to 90% stretchability of the SMNEA is significantly higher than those reported in other SMNEAs (Fig. 4D) (17, 20, 29, 30, 36, 48–51). Microneedle electrode arrays with 40 to 45% stretchability have been reported using more rigid microneedle materials such as silicon or stainless steel (17, 30); however, the microneedle array is either non-addressable or requires manual assembly. The stretchability of SMNEA can be further improved by optimizing the design of the serpentine interconnects (52). Figure S17 shows the FEA results of a design with approximately 100% stretchability by reducing the serpentine linewidth and increasing the spacing between microneedles. The Young's modulus of the PI microneedle ensures insertion into soft tissues without buckling while also offering a smaller mechanical mismatch compared to metal and silicon microneedles,

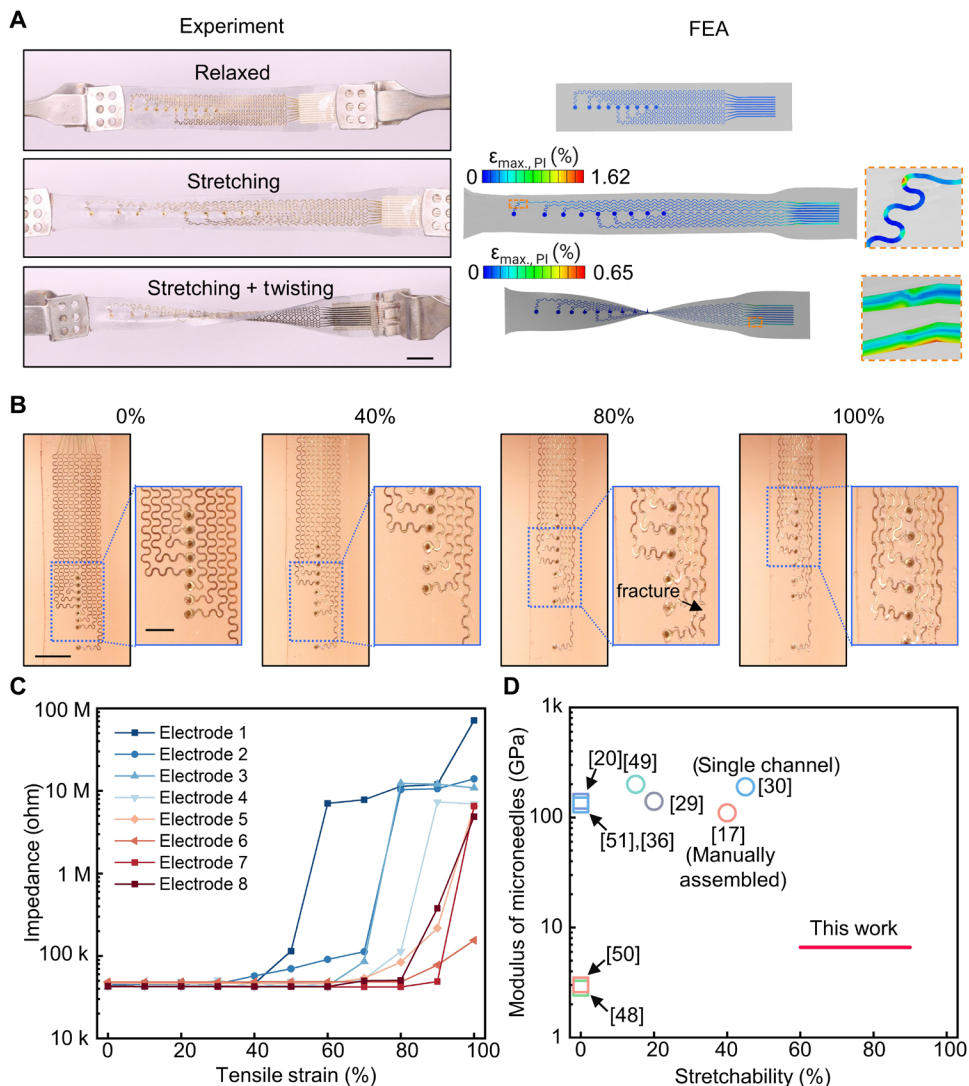


**Fig. 4. Stretchability of SMNEAs.** (A) Optical images and the corresponding FEA results showing the maximum principal strain distribution in the PI of an SMNEA device in relaxed state, under stretching, and under a combination of stretching and twisting. Insets show the locations of the maximum values of the maximum principal strain distributions. (B) Side-view optical images of an SMNEA device under uniaxial stretching up to 100%. (C) Impedance of the electrodes in the SMNEA device as a function of the tensile strain applied. (D) Comparison of the SMNEA in this work with previously reported flexible or stretchable microneedle electrode arrays in the microneedle modulus and the device stretchability. Scale bars, 5 mm [A and B (left)] and 2 mm [B (right)].

thus reducing potential tissue damage (53). The fabrication scheme presented here may be applied to materials with a higher modulus to create microneedles for stiffer target tissues, such as polymer composites (54) or metals via electroplating (55).

#### Ex vivo recording of intramuscular EMG

Large stretchability combined with relatively high modulus of the microneedles make SMNEA platforms well suited for recording electrophysiological signals within dynamically moving tissues, such as intramuscular EMG. The buccal mass of the marine mollusk *Aplysia californica* represents a model that contains a dense assembly of distinct muscle groups responsible for feeding (56), biting, and swallowing (57). We demonstrate the application of the SMNEA for sensing intramuscular EMGs from an isolated, dynamic buccal mass of *Aplysia*.

Muscle groups I1/I3 and I2 and a passive hinge are the main components of the buccal mass and they work together to compress the radula/odontophore (the toothed tongue and the muscle that moves it) for feeding (58). In a retraction cycle schematically shown in Fig. 5A, the I2 muscle relaxes and the I1/I3 muscles contract to push the radula/odontophore backward. As a result, the radular surface rotates posteriorly, approaching the entrance of the esophagus. Later, the radula/odontophore rotates back to its original position when I1/I3 and I2 muscles are all relaxing, and the buccal mass recovers to the rest status (56, 58).

An eight-channel SMNEA device with varying microneedle lengths (0.4 to 1.5 mm) is attached on an isolated buccal mass longitudinally with the microneedle electrodes inserted into the muscle tissues (Fig. 5B). The application of a hydrogel-based bioadhesive (59) between the SMNEA and the buccal mass surface ensures

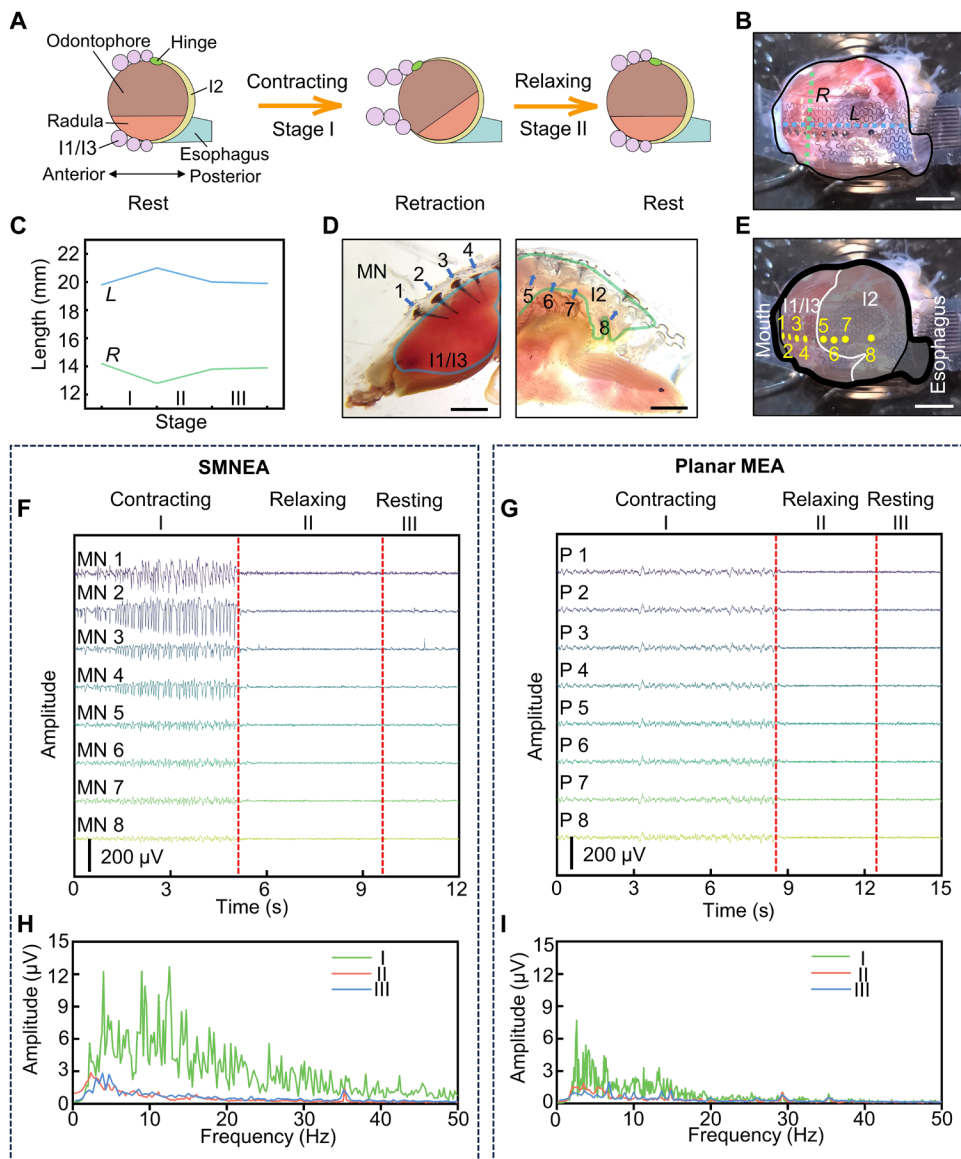


**Fig. 5. Ex vivo recordings of intramuscular and surface EMG from the buccal mass of *Aplysia* using SMNEA and planar MEA devices.** (A) Schematic illustration of a retraction movement cycle in the buccal mass. (B and C) Optical image of a buccal mass with an SMNEA device and the corresponding dimensional changes during a retraction movement cycle. *R* represents the diameter of the buccal mass at the anterior, and *L* represents the length from the mouth to the esophagus. (D) Confocal microscopic images showing the microneedle electrodes inserted into the I1/I3 and I2 muscle groups of the buccal mass. (E) Optical image with identification of each microneedle electrode inserted into the buccal mass. (F and G) Intramuscular EMG and surface EMG signals recorded by (F) the SMNEA and (G) the planar MEA, respectively. MN, microneedle electrodes; P, planar electrodes. (H and I) Power spectra of the intramuscular EMG and surface EMG signals averaged across all recording channels from (H) the SMNEA and (I) the planar MEA. Scale bars, 5 mm (B and E) and 2 mm (D).

stable device adhesion to the buccal mass. During a typical cycle of retraction movement, there exist three distinct stages: contracting, relaxing, and resting (Fig. 5A, fig. S18A, and movie S8). In the first stage (stage I), the anterior buccal mass retracts with the I1/I3 muscles contracting and the I2 muscle relaxing. As a result, the diameter at the anterior end (*R*) decreases, while the length from the mouth to the esophagus (*L*) increases (Fig. 5C). In stage II, the anterior buccal mass expands as I1/I3 and I2 muscles relax, causing opposite changes in *L* and *R*. In stage III, the buccal mass is in a resting state with both the I1/I3 and I2 muscle groups relaxed. The stretchable

SMNEA follows the deformations of the buccal mass throughout the movement cycle. After the recording experiments, the locations of the microneedle electrodes and the specific muscle groups are identified via preparation and conformal microscopic imaging of the buccal mass slice containing the microneedle electrodes (Fig. 5D; details are provided in Materials and Methods). Relatively long microneedle electrodes (~1.5 mm in length) numbered 1 to 4 are inserted into the I1/I3 muscle, and short microneedle electrodes 5 to 8 (~0.4 to 0.8 mm in length) are in the I2 muscle (Fig. 5E), with their exposed tips being the active recording sites.

The recorded intramuscular EMG signals from the electrodes 1 to 4 of the SMNEA (Fig. 5F) and the corresponding power spectral density graph (fig. S19A) show significantly higher amplitude than those recorded from electrodes 5 to 8 in stage I, when the I1/I3 muscles are contracting and I2 muscle is relaxing. The amplitude of the EMG signals decreases in stage II and stage III, where both the I1/I3 and I2 muscles are relaxed. The power spectrum analysis in Fig. 5H shows peak amplitudes centered around 5 to 20 Hz in stage I, characteristic of intramuscular EMG in *Aplysia* (60).

Planar MEAs are commonly used for electrophysiological sensing where they are attached to the surface of biotissues for recording biopotentials propagated to the surface, different from localized recording from the interior of tissues using SMNEA. For comparison, we perform recordings using a planar, thin-film MEA device with 600- $\mu\text{m}$ -diameter electrode size (figs. S20 and S21A; fabrication details appear in Materials and Methods) attached on the buccal mass of an *Aplysia* with a similar size and in similar regions of the surface as in the SMNEA experiments. The muscle movements during the recording process represent a retraction action similar to those in the recordings using SMNEA (figs. S18B and S21B and movie S9). Planar electrodes numbered 1 to 4 are attached on the surface of I1/I3 muscles, and electrodes 5 to 8 are attached on the I2 muscle's surface (fig. S21C). Different from the intramuscular EMG recorded using the SMNEA, the surface EMG recordings in Fig. 5G show relatively weak and similar EMG signals across all the planar electrodes in stage I. This may be explained by the difference between intramuscular EMG and surface EMG, with the latter sensing signals from multiple muscle groups underneath across certain depths (61, 62). The energy spectrum density graph of the surface EMG data in fig. S19B shows a lower frequency distribution (3 to 7 Hz from Fig. 5I) relative to the highly localized intramuscular EMG signals recorded by the SMNEA. This is likely due to the attenuation of EMG signals passing through tissues (63) and cross-talk from adjacent or deep muscles captured by the planar MEA (64–66).

The distinct features of the intramuscular and surface EMG recorded by the SMNEA and the planar MEA suggest that highly localized recording is necessary to probe electrical activities at the individual muscle level. Penetrating microneedle electrodes with different lengths and exposed microscale tips can target the interior of tissues, while the stretchability of the SMNEA device allows stable electrode-tissue interfacing during movements, contributing to higher signal-to-noise ratio. Thus, these attributes make SMNEA a useful tool for sensing or stimulating deep tissue in dynamic systems, to assist biological and neuroscience studies.

## DISCUSSION

In this study, we present a scalable fabrication method for creating microneedle electrode arrays with high device stretchability and customization. The unique combination of laser micromachining, molding, microfabrication, and transfer printing allows the realization of individually addressable microneedle electrodes with various geometries and array layouts, as well as large mechanical stretchability. A gel-assisted chemical etching process enables convenient control over the localized active electrode regions. The customization of electrode configuration is desirable for targeted sensing or stimulation. For example, these penetrating electrodes with spatially controlled lengths could reach different depths across multiple

layers of the brain's cortical circuit structure (67) or provide access to individual fascicles for selective stimulation of the peripheral nerves (68). The relatively high microneedle modulus enables robust insertion into target tissues, and the stretchability of the electrode arrays ensures intimate biointerfacing to soft, dynamically moving tissues in a minimally invasive manner. These attributes make the SMNEA a promising platform for ex vivo or in vivo sensing or stimulation in the interior of biological tissues, as demonstrated in the example of intramuscular EMG recording in the buccal mass of *Aplysia*. This SMNEA platform may find applications in electrophysiological sensing in brain-machine interfaces (29, 67), electrochemical sensing of skin interstitial fluids (69), and electrical stimulation of nerves (70) and muscles (17, 71). Higher electrode density is achievable by optimizing the serpentine interconnects. The softness and stretchability of the SMNEA make it potentially suitable for measuring dynamic tissues with large and fast deformations and for long-term use, which may require stable interface adhesion to target tissues (30, 72). The penetrating and stretchable microneedle arrays can also be integrated with advanced sensors, optics, optoelectronics, and microfluidics for a diverse range of sensing and modulation functions, including extraction of body fluids (73), light guide-assisted optical therapy (22), optogenetics (74), and targeted drug delivery (75, 76).

## MATERIALS AND METHODS

### Replica molding of PI microneedles

Fabrication of the stretchable microneedles began with curing (80°C for 2 hours) a sheet of PDMS (Dow Sylgard 184) (10:1 mixing ratio, 2 mm in thickness), followed by ultraviolet (UV) ozone treatment (270 s) of the cured PDMS surface and bonding of the treated surface to a glass slide. Laser ablation of the PDMS using a low-cost CO<sub>2</sub> laser cutter (Universal Laser System PLS) created conical cavities in the PDMS, which served as the molds. Circular ablation patterns (repeated twice) were used with 17% power and 15% speed. Preparation of the PDMS molds for microneedle molding started with cleaning of the PDMS molds with sonication (5 min) in isopropyl alcohol (IPA), followed by immersion (2 min) in 3-aminopropyltriethoxysilane (0.01% in IPA solution), drying, and corona treatment (Electro-Technic Products) of the surface for 30 s to improve the surface wettability and adhesion to PI. Initial deposition of liquid PI-2610 precursors (HD Microsystems) onto the mold filled the cavities, assisted by vacuum degassing (30 min). Deposition of additional PI-2610 precursors onto the molds further removed air bubbles, followed by spin coating (600 rpm for 30 s) and a multistep curing process (35°C for 1 hour, 50°C for 1 hour, 80°C for 1 hour, 110°C for 1 hour, and 230°C for 4 hours) in an oven to form a thin PI film.

### Fabrication of stretchable microneedle electrodes

Patterning of the thin PI film formed in the replica molding process started with deposition and lithographically patterned etching of a Cu hard mask (200 nm in thickness) on the cured PI film. The hard mask transferred the layouts of circular shaped microneedle bases and serpentine interconnects to the PI layer via oxygen plasma etching (March RIE) of the PI to form patterned gaps (30  $\mu\text{m}$  in width) that separate the microneedle bases and serpentine interconnects from the rest of the PI film. After the removal of the hard mask in a Cu etchant, a lithography step defined a sacrificial photoresist (AZ

5214) layer on the PI film outside the microneedle bases and serpentine filaments. Dispensing the photoresist over the entire surface before spin coating ensured complete photoresist coverage across the gaps. Subsequently, a sputtering deposition of Ti/SiO<sub>2</sub> (10 nm/50 nm in thickness) created the bonding layer. Separately, a silicone film (Ecoflex 0030, Smooth-On Inc.; approximately 200 μm in thickness) spin-coated and cured on a PI film (50 μm in thickness) served as the stretchable substrate for the SMNEA. Transfer of the PI from the PDMS mold to the Ecoflex substrate began with UV ozone treatment of the Ecoflex and corona treatment of the PI surface to create hydroxyl groups on the surfaces. Laminating the PI/PDMS onto the Ecoflex substrate and heating (70°C for 10 min) led to strong covalent bonding. Immersion of the bonded PI in IPA facilitated the peeling of the PI from the PDMS mold. After successful transfer of the PI to an Ecoflex substrate, sputter deposition of a layer of Cr/Au (10 nm/150 nm in thickness) metallized the microneedles and the serpentine filaments. Immersion of the sample in acetone undercut the sacrificial photoresist layer. Peeling of the PI film outside of the microneedle bases and serpentine filaments from the Ecoflex substrate completed the process, facilitated by the patterned sacrificial layer between the PI and the Ti/SiO<sub>2</sub> bonding layer.

### Fabrication of stretchable planar electrodes

Fabrication of the stretchable planar electrodes began with spin coating (3000 rpm for 30 s) a sacrificial layer of polymethyl methacrylate (PMMA) on a glass slide, followed by spin coating (1500 rpm for 40 s) of PI-2545 (HD Microsystems; 4 μm in thickness). Deposition, patterning, and etching of a metal layer (Cr/Au; 10 nm/300 nm in thickness) defined the electrode areas and the serpentine traces. Spin coating of another PI-2545 layer (1500 rpm for 40 s) formed the top encapsulation layer. A lithographic patterning step and subsequent etching using oxygen plasma (March RIE) defined the outline of the serpentine and exposed the metal electrodes, as well as the contact pads for electrical connection. Undercutting the PMMA sacrificial layer in acetone facilitated the transfer of the planar electrodes from the glass slide to a water-soluble tape (polyvinyl alcohol). Deposition of Ti/SiO<sub>2</sub> (10 nm/50 nm in thickness) on the back side of the planar electrodes allowed covalent bonding to a separate silicone film (Ecoflex, 200 μm in thickness) following the same steps described in the fabrication of stretchable microneedle electrodes.

### Controlled exposure of microneedle conductive tips

The process began with conformal coating (Specialty Coating Systems, PDS 2010) of an insulating parylene C (3 μm in thickness) on the SMNEA. Then, a thin Cu layer (200 nm in thickness) sputter-coated through a shadow mask covered the sidewalls of the microneedles, serving as a hard mask for tip exposure. Separately, a gel etchant was prepared by soaking an agarose gel (0.6 g in 100 ml of deionized water; Sigma-Aldrich) in diluted copper etchant (FeCl<sub>3</sub>/HCl, 1:20 dilution; Sigma-Aldrich) for 8 hours. Brief (approximately 5 s) insertion of the Cu-coated microneedle tips in this gel etchant removed the Cu hard mask at the tips. Control of the microneedle insertion length relied on a high-precision linear stage (VT 80, Physik Instrumente) to which the microneedles were attached with side-view microscopic imaging (Keyence). Following the selective removal of the Cu hard mask at the microneedle tips, an oxygen plasma etching removed the exposed parylene C not covered by the

hard mask and the remaining SiO<sub>2</sub> layer. Removal of the hard mask in liquid Cu etchant completed the patterning of the insulation coating. An additional spin coating of Ecoflex (approximately 200 μm in thickness) on the SMNEA device provided encapsulation of the serpentine interconnects and the microneedle bases after electrical connection between the contact pads and anisotropic conductive film cables.

### Impedance measurements and electrochemical deposition

Impedance measurements and electrochemical deposition relied on a potentiostat and impedance analyzer (PalmSens4) with a Pt electrode as the counter electrode and Ag/AgCl as the reference electrode. Impedance measurements were conducted in PBS (pH 7.4) with scanning frequencies from 5 to 10 kHz. Electrochemical deposition of PtB used a mixture of 0.6 g of chloroplatinic acid (PtCl<sub>6</sub>H<sub>2</sub>; Sigma-Aldrich), 5 mg of lead acetate [Pb(C<sub>2</sub>H<sub>3</sub>O<sub>2</sub>)<sub>2</sub>; Sigma-Aldrich], and 20 ml of deionized water using chronoamperometry (−0.1 V for 20 s).

### Mechanical characterization

A PI-2610 film (30 μm in thickness) prepared using procedures similar to those used in the fabrication of SMNEAs served as a sample for mechanical characterization. Uniaxial tensile testing (Mark-10) of a dog bone-shaped specimen according to the ASTM D638 standard patterned by laser ablation yielded force versus displacement data. The Young's modulus was calculated from a linear fitting of the stress-strain curve within the linear regime.

### Indentation and insertion tests of microneedles

A linear stage (VT 80, Physik Instrumente) connected to a force gauge (Mark-10) drove an indenter or a PDMS cube (10:1 mixing ratio) toward the microneedles to a displacement of 1 mm. For repeated insertion tests, the microneedles were inserted into PDMS (20:1 mixing ratio) or agarose gel with an insertion depth of 0.8 mm. Impedance measurements of the microneedle electrodes were performed after the 1st, 5th, 10th, 20th, 50th, 100th, and 1000th insertions.

### Characterization of the stretchability of SMNEAs

Attaching one end of the SMNEA device to a motorized force tester (Mark-10) and keeping the other end fixed with the microneedle electrodes immersed in PBS (pH 7.4) allowed impedance measurements of the electrodes with different tensile strain. Impedance measurements were taken for increments of 10% elongation.

### Finite element analysis

Simulations for the SMNEAs were conducted by the commercial software ABAQUS. The structure was meshed using eight-node 3D stress solid elements (C3D8R) with a fine element size (~100,000 elements) smaller than the serpentine width to ensure accuracy. The stretching and twisting deformations were applied by corresponding translation or rotation displacements on the two ends of the SMNEA sample. The materials were described by different constitutive models including a linear elastic model for PI and Au and a Mooney-Rivlin hyper-elastic model for Ecoflex. The Young's moduli of PI-2610 and Au are  $E_{PI} = 6.63$  GPa and  $E_{Au} = 79$  GPa, respectively. The Poisson's ratios are  $\nu_{PI} = 0.4$  and  $\nu_{Au} = 0.44$ , respectively. The yield stress of the Au is 546 MPa [corresponding strain is 0.7% for Au thin films (47)]. The Mooney-Rivlin strain potential of Ecoflex is governed by

$$U = C_{10}(\bar{I}_1 - 3) + C_{01}(\bar{I}_2 - 3) + D_1^{-1}(J^{el} - 1)^2$$

where  $C_{10} = 0.008054 \text{ MPa}$ ,  $C_{01} = 0.002013 \text{ MPa}$ , and  $D_1 = 2.0 \text{ MPa}^{-1}$ .  $\bar{I}_1$  and  $\bar{I}_2$  are the first and the second invariants of the deviatoric strain tensor, and  $J^{\text{el}}$  is the elastic volume ratio representing the thermal expansion.

The simulation of the buckling behaviors of microneedles was conducted in ABAQUS. C3D8R elements were used to mesh the structure with an element size of  $\sim 9 \mu\text{m}$  ( $\sim 31,000$  elements). The base of the microneedles was fixed, and the tip surface was coupled to a reference point with a vertical unit force applied to it. The buckling analysis generated the critical forces and the corresponding deformation modes.

### Ex vivo EMG recording in *Aplysia*

Specimens of *A. californica* (California sea hare) were obtained from the National Institutes of Health National Resource for *Aplysia*, University of Miami, Florida, shipped overnight, and housed in closed circulation aquaria with artificial seawater (Instant Ocean) at  $12^\circ\text{C}$ . The *Aplysia* specimens were cold anesthetized at  $4^\circ\text{C}$  for at least 30 min. Separately, strips of dry hydrogel-based adhesive patch were prepared (59) and later applied between the SMNEA and the buccal mass surface. The buccal mass with buccal ganglia were dissected out of each *Aplysia* specimen in artificial sea water and placed in a petri dish covered by a PDMS layer, with pins applied at the mouth or esophagus of the buccal mass, if necessary, to stabilize its position. The SMNEA was then placed on the buccal mass longitudinally and held for  $\sim 20$  s to ensure microneedle electrode insertion as well as adhesion of the hydrogel to both the SMNEA and the buccal mass surface. Subsequently, the petri dish with buccal mass was filled with room temperature saline (420 mM NaCl, 10 mM KCl, 25 mM MgCl<sub>2</sub>, 25 mM MgSO<sub>4</sub>, 10 mM CaCl<sub>2</sub>, and 10 mM Hepes, adjusted to pH 7.6 with NaOH). Electrophysiological recordings were digitized with a sampling rate of 20 kS/s using a head-stage (Intan RHD 32-channel) and an acquisition board (Open Ephys). The bandwidth of the amplifier hardware extended from 0.1 to 7600 Hz, and a digital bandpass filter of 3 to 3000 Hz eliminated high-frequency noise and smoothed the signal. A notch filter at 60 Hz further reduced the noise signals from the power line. Movies were recorded using a camera, synchronized with the electrophysiological recordings by capturing the flashing of a light-emitting diode coupled with a 5-V stimulator. Movements of the buccal mass were spontaneous or initiated via tactile stimulation of the esophagus with forceps.

### Slicing and imaging

After EMG recording, the buccal mass with inserted microneedle electrodes was placed in the freezer in a dish of saline and kept at  $-18^\circ\text{C}$  until it was fully frozen. Feather razor blades were used to make two longitudinal cuts as close as possible to the microneedle electrodes. The thin longitudinal slice was placed onto a glass cover-slip and imaged under a confocal microscope with high intensity backlight to identify microneedle electrode locations. If needed, the slice was flipped to the other side to obtain clearer images of other microneedle electrode locations.

### Supplementary Materials

This PDF file includes:

Figs. S1 to S21

Table S1

Legends for movies S1 to S9

**Other Supplementary Material for this manuscript includes the following:**  
Movies S1 to S9

### REFERENCES AND NOTES

- M. E. J. Obien, K. Deligkaris, T. Bullmann, D. J. Bakkum, U. Frey, Revealing neuronal function through microelectrode array recordings. *Front. Neurosci.* **8**, 423 (2015).
- L. Ren, B. Liu, W. Zhou, L. Jiang, A mini review of microneedle array electrode for bio-signal recording: a review. *IEEE Sens. J.* **20**, 577–590 (2020).
- K. Ino, H. Shiku, T. Matsue, Bioelectrochemical applications of microelectrode arrays in cell analysis and engineering. *Curr. Opin. Electrochem.* **5**, 146–151 (2017).
- W. Gao, H. Y. Y. Nyein, Z. Shahpar, H. M. Fahad, K. Chen, S. Emamnejad, Y. Gao, L.-C. Tai, H. Ota, E. Wu, J. Bullock, Y. Zeng, D.-H. Lien, A. Javey, Wearable microsensor array for multiplexed heavy metal monitoring of body fluids. *ACS Sens.* **1**, 866–874 (2016).
- Z. Aqrawe, J. Montgomery, J. Travas-Sejdic, D. Svirskis, Conducting polymers for neuronal microelectrode array recording and stimulation. *Sens. Actuators B Chem.* **257**, 753–765 (2018).
- S.-H. Sunwoo, M.-J. Cha, S. I. Han, H. Kang, Y. S. Cho, D.-H. Yeom, C. S. Park, N. K. Park, S. W. Choi, S. J. Kim, G. D. Cha, D. Jung, S. Choi, S. Oh, G.-B. Nam, T. Hyeon, D.-H. Kim, S.-P. Lee, Ventricular tachyarrhythmia treatment and prevention by subthreshold stimulation with stretchable epicardial multichannel electrode array. *Sci. Adv.* **9**, eadff6856 (2023).
- P. Pochay, K. D. Wise, L. F. Allard, L. T. Rutledge, A multichannel depth probe fabricated using electron-beam lithography. *Biomed. Eng.* **BME-26**, 199–206 (1979).
- C. M. Didier, A. Kundu, D. DeRoo, S. Rajaraman, Development of in vitro 2D and 3D microelectrode arrays and their role in advancing biomedical research. *J. Micromech. Microeng.* **30**, 103001 (2020).
- Y. Jimbo, D. Sasaki, T. Ohya, S. Lee, W. Lee, F. Arab Hassani, T. Yokota, K. Matsuura, S. Umezawa, T. Shimizu, T. Someya, An organic transistor matrix for multipoint intracellular action potential recording. *Proc. Natl. Acad. Sci. U.S.A.* **118**, e2022300118 (2021).
- A. B. Schwartz, Cortical neural prosthetics. *Annu. Rev. Neurosci.* **27**, 487–507 (2004).
- A. C. Hoogerwerf, K. D. Wise, A three-dimensional microelectrode array for chronic neural recording. *IEEE Trans. Biomed. Eng.* **41**, 1136–1146 (1994).
- H. Shin, S. Jeong, J.-H. Lee, W. Sun, N. Choi, I.-J. Cho, 3D high-density microelectrode array with optical stimulation and drug delivery for investigating neural circuit dynamics. *Nat. Commun.* **12**, 492 (2021).
- M. S. Saleh, S. M. Ritchie, M. A. Nicholas, H. L. Gordon, C. Hu, S. Jahan, B. Yuan, R. Bezarra, J. W. Reddy, Z. Ahmed, M. Chamanzar, E. A. Yttri, R. P. Panat, CMU Array: A 3D nanoprinted, fully customizable high-density microelectrode array platform. *Sci. Adv.* **8**, eabj4853 (2022).
- M. M. H. Shandhi, S. Negi, Fabrication of out-of-plane high channel density microelectrode neural array with 3D recording and stimulation capabilities. *J. Microelectromech. Syst.* **29**, 522–531 (2020).
- M. Parrilla, A. Vanhooydonck, M. Johns, R. Watts, K. De Wael, 3D-printed microneedle-based potentiometric sensor for pH monitoring in skin interstitial fluid. *Sens. Actuators B Chem.* **378**, 133159 (2023).
- P. Wijdenes, K. Haider, C. Gavrilovici, B. Gunning, M. D. Wolff, T. Lijnse, R. Armstrong, G. C. Teskey, J. M. Rho, C. Dalton, N. I. Syed, Three dimensional microelectrodes enable high signal and spatial resolution for neural seizure recordings in brain slices and freely behaving animals. *Sci. Rep.* **11**, 21952 (2021).
- G. S. Guvanasen, L. Guo, R. J. Aguilar, A. L. Cheek, C. S. Shafor, S. Rajaraman, T. R. Nichols, S. P. DeWeerth, A stretchable microneedle electrode array for stimulating and measuring intramuscular electromyographic activity. *IEEE Trans. Neural Syst. Rehabil. Eng.* **25**, 1440–1452 (2016).
- H. Zhao, Y. Kim, H. Wang, X. Ning, C. Xu, J. Suh, M. Han, G. J. Pagan-Diaz, W. Lu, H. Li, W. Bai, O. Aydin, Y. Park, J. Wang, Y. Yao, Y. He, M. T. A. Saif, Y. Huang, R. Bashir, J. A. Rogers, Compliant 3D frameworks instrumented with strain sensors for characterization of millimeter-scale engineered muscle tissues. *Proc. Natl. Acad. Sci. U.S.A.* **118**, e2100077118 (2021).
- Y. Park, C. K. Franz, H. Ryu, H. Luan, K. Y. Cotton, J. U. Kim, T. S. Chung, S. Zhao, A. Vazquez-Guardado, D. S. Yang, K. Li, R. Avila, J. K. Phillips, M. J. Quezada, H. Jang, S. S. Kwak, S. M. Won, K. Kwon, H. Jeong, A. J. Bandodkar, M. Han, H. Zhao, G. R. Osher, H. Wang, K. Lee, Y. Zhang, Y. Huang, J. D. Finan, J. A. Rogers, Three-dimensional, multifunctional neural interfaces for cortical spheroids and engineered assembloids. *Sci. Adv.* **7**, eabf9153 (2021).
- Z. Wei, S. Zheng, R. Wang, X. Bu, H. Ma, Y. Wu, L. Zhu, Z. Hu, Z. Liang, Z. Li, A flexible microneedle array as low-voltage electroporation electrodes for in vivo DNA and siRNA delivery. *Lab Chip* **14**, 4093–4102 (2014).
- M. Mahmood, S. Kwon, H. Kim, Y.-S. Kim, P. Siriaraya, J. Choi, B. Otkhmezuri, K. Kang, K. J. Yu, Y. C. Jang, C. S. Ang, W.-H. Yeo, Wireless soft scalp electronics and virtual reality system for motor imagery-based brain-machine interfaces. *Adv. Sci.* **8**, 2101129 (2021).

22. H. Zhang, H. Zhao, X. Zhao, C. Xu, D. Franklin, A. Vázquez-Guardado, W. Bai, J. Zhao, K. Li, G. Monti, W. Lu, A. Kobeissi, L. Tian, X. Ning, X. Yu, S. Mehta, D. Chanda, Y. Huang, S. Xu, B. E. Perez White, J. A. Rogers, Biocompatible light guide-assisted wearable devices for enhanced UV light delivery in deep skin. *Adv. Funct. Mater.* **31**, 2100576 (2021).
23. L. Ren, S. Xu, J. Gao, Z. Lin, Z. Chen, B. Liu, L. Liang, L. Jiang, Fabrication of flexible microneedle array electrodes for wearable bio-signal recording. *Sensors* **18**, 1191 (2018).
24. K. Sim, Z. Rao, Y. Li, D. Yang, C. Yu, Curvy surface conformal ultra-thin transfer printed Si optoelectronic penetrating microprobe arrays. *Npj Flex. Electron.* **2**, 2 (2018).
25. D. A. Soscia, D. Lam, A. C. Tooker, H. A. Enright, M. Triplett, P. Karande, S. K. G. Peters, A. P. Sales, E. K. Wheeler, N. O. Fischer, A flexible 3-dimensional microelectrode array for in vitro brain models. *Lab Chip* **20**, 901–911 (2020).
26. V. Mor-Avi, R. M. Lang, L. P. Badano, M. Belohlavek, N. M. Cardim, G. Derumeaux, M. Galderisi, T. Marwick, S. F. Nagueh, P. P. Sengupta, R. Sicari, O. A. Smiseth, B. Smulevitz, M. Takeuchi, J. D. Thomas, M. Vannan, J.-U. Voigt, J. L. Zamorano, Current and evolving echocardiographic techniques for the quantitative evaluation of cardiac mechanics: ASE/EAE consensus statement on methodology and indications endorsed by the Japanese Society of Echocardiography. *Eur. J. Echocardiogr.* **12**, 167–205 (2011).
27. R. G. P. Lopata, J. P. van Dijk, S. Pillen, M. M. Nillesen, H. Maas, J. M. Thijssen, D. F. Stegeman, C. L. de Korte, Dynamic imaging of skeletal muscle contraction in three orthogonal directions. *J. Appl. Physiol.* **109**, 906–915 (2010).
28. S. Liu, Y. Rao, H. Jang, P. Tan, N. Lu, Strategies for body-conformable electronics. *Matter* **5**, 1104–1136 (2022).
29. D. Yan, A. A. Jiman, E. C. Bottorff, P. R. Patel, D. Meli, E. J. Welle, D. C. Ratze, L. A. Hayton, C. A. Chestek, S. W. P. Kemp, T. M. Bruns, E. Yoon, J. P. Seymour, Ultraflexible and stretchable intrafascicular peripheral nerve recording device with axon-dimension, cuff-less microneedle electrode array. *Small* **18**, 2200311 (2022).
30. H. Ji, M. Wang, Y. Wang, Z. Wang, Y. Ma, L. Liu, H. Zhou, Z. Xu, X. Wang, Y. Chen, X. Feng, Skin-integrated, biocompatible, and stretchable silicon microneedle electrode for long-term EMG monitoring in motion scenario. *Npj Flex. Electron.* **7**, 46 (2023).
31. Y. Zhang, S. Wang, X. Li, J. A. Fan, S. Xu, Y. M. Song, K.-J. Choi, W.-H. Yeo, W. Lee, S. N. Nazaar, B. Lu, L. Yin, K.-C. Hwang, J. A. Rogers, Y. Huang, Experimental and theoretical studies of serpentine microstructures bonded to prestrained elastomers for stretchable electronics. *Adv. Funct. Mater.* **24**, 2028–2037 (2014).
32. H. Zhao, X. Cheng, C. Wu, T.-L. Liu, Q. Zhao, S. Li, X. Ni, S. Yao, M. Han, Y. Huang, Y. Zhang, J. A. Rogers, Mechanically guided hierarchical assembly of 3D mesostructures. *Adv. Mater.* **34**, 2109416 (2022).
33. X. Huang, L. Liu, Y. H. Lin, R. Feng, Y. Shen, Y. Chang, H. Zhao, High-stretchability and low-hysteresis strain sensors using origami-inspired 3D mesostructures. *Sci. Adv.* **9**, eadh9799 (2023).
34. S. Idogawa, K. Yamashita, Y. Kubota, H. Sawahata, R. Sanda, S. Yamagiwa, R. Numano, K. Koida, T. Kawano, Coaxial microneedle-electrode for multichannel and local-differential recordings of neuronal activity. *Sens. Actuators B Chem.* **320**, 128442 (2020).
35. B.-R. Maeng, K.-T. Nam, S.-K. Lee, J.-H. Park, Fabrication and measurement of microtip electrode array with self-aligned integrated dual conductive electrodes. *Sens. Actuators B Chem.* **237**, 1015–1020 (2016).
36. S. H. Lee, M. Thunemann, K. Lee, D. R. Cleary, K. J. Tonsfeldt, H. Oh, F. Azzazy, Y. Tchoe, A. M. Bourhis, L. Hossain, Y. G. Ro, A. Tanaka, K. Kilic, A. Devor, S. A. Dayeh, Scalable thousand channel penetrating microneedle arrays on flex for multimodal and large area coverage brainmachine interfaces. *Adv. Funct. Mater.* **32**, 2112045 (2022).
37. M. A. Brown, K. M. Zappitelli, L. Singh, R. C. Yuan, M. Bemrose, V. Brodgen, D. J. Miller, M. C. Smear, S. F. Cogan, T. J. Gardner, Direct laser writing of 3D electrodes on flexible substrates. *Nat. Commun.* **14**, 3610 (2023).
38. J. Li, D. Huang, Y. Chen, Z. Li, Low-cost, metal-based micro-needle electrode array (M-MNEA): a three-dimensional intracortical neural interface. *2019 20th International Conference on Solid-State Sensors, Actuators and Microsystems & Eurosensors XXXIII (TRANSDUCERS & EUROSENSORS XXXIII)* (IEEE, 2019), pp. 1635–1638.
39. D. Byun, S. J. Cho, S. Kim, Fabrication of a flexible penetrating microelectrode array for use on curved surfaces of neural tissues. *J. Micromech. Microeng.* **23**, 125010 (2013).
40. C. Barrett, F. O'Sullivan, S. Barry, K. Grygorjev, D. O'Gorman, C. O'Mahony, A. O'Riordan, Novel surface modified polymer microneedle based biosensors for interstitial fluid glucose detection. in *2019 IEEE SENSORS* (IEEE, 2019), pp. 1–4.
41. C. Barrett, K. Dawson, C. O'Mahony, A. O'Riordan, Development of low cost rapid fabrication of sharp polymer microneedles for in vivo glucose biosensing applications. *ECS J. Solid State Sci. Technol.* **4**, S3053–S3058 (2015).
42. W. Pei, H. Zhang, Y. Wang, X. Guo, X. Xing, Y. Huang, Y. Xie, X. Yang, H. Chen, Skin-potential variation insensitive dry electrodes for ECG recording. *IEEE Trans. Biomed. Eng.* **64**, 463–470 (2016).
43. D. E. Gunning, J. M. Beggs, W. Dabrowski, P. Hottowy, C. J. Kenney, A. Sher, A. M. Litke, K. Mathieson, Dense arrays of micro-needles for recording and electrical stimulation of neural activity in acute brain slices. *J. Neural Eng.* **10**, 016007 (2013).
44. H. Zhao, C. Jacob, H. A. Stone, A. J. Hart, Liquid imbibition in ceramic-coated carbon nanotube films. *Langmuir* **32**, 12686–12692 (2016).
45. S. M. Darbandi, R. D. Firouz-Abadi, H. Haddadpour, Buckling of variable section columns under axial loading. *J. Eng. Mech.* **136**, 472–476 (2010).
46. X. Kong, P. Zhou, C. Wu, Numerical simulation of microneedles' insertion into skin. *Comput. Methods Biomed. Engin.* **14**, 827–835 (2011).
47. C. A. Neugebauer, Tensile properties of thin, evaporated gold films. *J. Appl. Phys.* **31**, 1096–1101 (1960).
48. C. Didier, A. Kundu, S. Rajaraman, Capabilities and limitations of 3D printed microserpentines and integrated 3D electrodes for stretchable and conformable biosensor applications. *Microsyst. Nanoeng.* **6**, 15 (2020).
49. L. Guo, G. Guvanasen, C. Tuthill, T. R. Nichols, S. P. DeWeert, A low-cost, easy-fabricating stretchable microneedle-electrode array for intramuscular recording and stimulation. *2011 5th International IEEE/EMBS Conference on Neural Engineering (IEEE, 2011)*, pp. 562–565.
50. W. Lee, S.-H. Jeong, Y.-W. Lim, H. Lee, J. Kang, H. Lee, I. Lee, H.-S. Han, S. Kobayashi, M. Tanaka, B.-S. Bae, Conformable microneedle pH sensors via the integration of two different siloxane polymers for mapping peripheral artery disease. *Sci. Adv.* **7**, eabi6290 (2021).
51. R. Wang, W. Zhao, W. Wang, Z. Li, A flexible microneedle electrode array with solid silicon needles. *J. Microelectromech. Syst.* **21**, 1084–1089 (2012).
52. T. Widlund, S. Yang, Y.-Y. Hsu, N. Lu, Stretchability and compliance of freestanding serpentine-shaped ribbons. *Int. J. Solids Struct.* **51**, 4026–4037 (2014).
53. A. Fujishiro, H. Kaneko, T. Kawashima, M. Ishida, T. Kawano, In vivo neuronal action potential recordings via three-dimensional microscale needle-electrode arrays. *Sci. Rep.* **4**, 4868 (2014).
54. I. Mansoor, U. O. Hafeli, B. Stoeber, Hollow out-of-plane polymer microneedles made by solvent casting for transdermal drug delivery. *J. Microelectromech. Syst.* **21**, 44–52 (2011).
55. P. R. Miller, M. Moorman, R. D. Boehm, S. Wolfley, V. Chavez, J. T. Baca, C. Ashley, I. Brener, R. J. Narayan, R. Polksky, Fabrication of hollow metal microneedle arrays using a molding and electroplating method. *MRS Adv.* **4**, 1417–1426 (2019).
56. G. P. Sutton, E. V. Mangan, D. M. Neustadter, R. D. Beer, P. E. Crago, H. J. Chiel, Neural control exploits changing mechanical advantage and context dependence to generate different feeding responses in Aplysia. *Biol. Cybern.* **91**, 333–345 (2004).
57. D. W. Morton, H. J. Chiel, In vivo buccal nerve activity that distinguishes ingestion from rejection can be used to predict behavioral transitions in Aplysia. *J. Comp. Physiol.* **172**, 17–32 (1993).
58. G. P. Sutton, J. B. Macknin, S. S. Gartman, G. P. Sunny, R. D. Beer, P. E. Crago, D. M. Neustadter, H. J. Chiel, Passive hinge forces in the feeding apparatus of Aplysia aid retraction during biting but not during swallowing. *J. Comp. Physiol.* **190**, 501–514 (2004).
59. J. Wu, H. Yuk, T. L. Sarrafian, C. F. Guo, L. G. Griffiths, C. S. Nabzdyk, X. Zhao, An off-the-shelf biodegradable patch for sutureless repair of gastrointestinal defects. *Sci. Transl. Med.* **14**, eab2857 (2022).
60. I. Hurwitz, D. Neustadter, D. W. Morton, H. J. Chiel, A. J. Susswein, Activity patterns of the B31/B32 pattern initiators innervating the I2 muscle of the buccal mass during normal feeding movements in Aplysia californica. *J. Neurophysiol.* **75**, 1309–1326 (1996).
61. S. H. Roy, C. J. De Luca, J. Schneider, Effects of electrode location on myoelectric conduction velocity and median frequency estimates. *J. Appl. Physiol.* **61**, 1510–1517 (1986).
62. D. Farina, F. Negro, Accessing the neural drive to muscle and translation to neurorehabilitation technologies. *IEEE Rev. Biomed. Eng.* **5**, 3–14 (2012).
63. J. Perry, C. S. Easterday, D. J. Antonelli, Surface versus intramuscular electrodes for electromyography of superficial and deep muscles. *Phys. Ther.* **61**, 7–15 (1981).
64. C. De Luca, The use of surface electromyography in biomechanics. *J. Appl. Biomech.* **13**, 135–163 (1997).
65. N. A. Dimitrova, G. V. Dimitrov, O. A. Nikitin, Neither high-pass filtering nor mathematical differentiation of the EMG signals can considerably reduce cross-talk. *J. Electromyogr. Kinesiol.* **12**, 235–246 (2002).
66. A. Péter, E. Andersson, A. Hegyi, T. Finni, O. Tarassova, N. Cronin, H. Grundström, A. Arndt, Comparing surface and fine-wire electromyography activity of lower leg muscles at different walking speeds. *Front. Physiol.* **10**, 1283 (2019).
67. A. V. Nurmiikk, J. P. Donoghue, L. R. Hochberg, W. R. Patterson, Y.-K. Song, C. W. Bull, D. A. Borton, F. Laiwalla, S. Park, Y. Ming, J. Aceros, Listening to brain microcircuits for interfacing with external world—progress in wireless implantable microelectronic neuroengineering devices. *Proc. IEEE* **98**, 375–388 (2010).
68. A. Branner, R. B. Stein, R. A. Normann, Selective stimulation of cat sciatic nerve using an array of varying-length microelectrodes. *J. Neurophysiol.* **85**, 1585–1594 (2001).
69. Z. Wang, J. Luan, A. Seth, L. Liu, M. You, P. Gupta, P. Rathi, Y. Wang, S. Cao, Q. Jiang, X. Zhang, R. Gupta, Q. Zhou, J. J. Morrissey, E. L. Scheller, J. S. Rudra, S. Singamaneni, Microneedle patch for the ultrasensitive quantification of protein biomarkers in interstitial fluid. *Nat. Biomed. Eng.* **5**, 64–76 (2021).
70. Y.-C. Chan, Y.-H. Lin, H.-C. Liu, R.-S. Hsu, M.-R. Chiang, L.-W. Wang, T.-C. Chou, T.-T. Lu, I.-C. Lee, L.-A. Chu, S.-H. Hu, In situ magnetoelectric generation of nitric oxide and electric stimulus for nerve therapy by wireless chargeable molybdenum carbide octahedrons. *Nano Today* **51**, 101935 (2023).

71. L. Xu, S. R. Gutbrod, A. P. Bonifas, Y. Su, M. S. Sulkin, N. Lu, H.-J. Chung, K.-I. Jang, Z. Liu, M. Ying, C. Lu, R. C. Webb, J.-S. Kim, J. I. Laughner, H. Cheng, Y. Liu, A. Ameen, J.-W. Jeong, G.-T. Kim, Y. Huang, I. R. Efimov, J. A. Rogers, 3D multifunctional integumentary membranes for spatiotemporal cardiac measurements and stimulation across the entire epicardium. *Nat. Commun.* **5**, 3329 (2014).
72. H. Kim, J. Lee, U. Heo, D. K. Jayashankar, K.-C. Agno, Y. Kim, C. Y. Kim, Y. Oh, S.-H. Byun, B. Choi, H. Jeong, W.-H. Yeo, Z. Li, S. Park, J. Xiao, J. Kim, J.-W. Jeong, Skin preparation-free, stretchable microneedle adhesive patches for reliable electrophysiological sensing and exoskeleton robot control. *Sci. Adv.* **10**, eadk5260 (2024).
73. M. R. Sarabi, A. Ahmadpour, A. K. Yetisen, S. Tasoglu, Finger-actuated microneedle array for sampling body fluids. *Appl. Sci.* **11**, 5329 (2021).
74. K. Y. Kwon, H.-M. Lee, M. Ghovanloo, A. Weber, W. Li, Design, fabrication, and packaging of an integrated, wirelessly-powered optrode array for optogenetics application. *Front. Syst. Neurosci.* **9**, 69 (2015).
75. C. Yeung, S. Chen, B. King, H. Lin, K. King, F. Akhtar, G. Diaz, B. Wang, J. Zhu, W. Sun, A. Khademhosseini, S. Emaminejad, A 3D-printed microfluidic-enabled hollow microneedle architecture for transdermal drug delivery. *Biomicrofluidics* **13**, 064125 (2019).
76. Z. Wang, J. Wang, H. Li, J. Yu, G. Chen, A. R. Kahkoska, V. Wu, Y. Zeng, D. Wen, J. R. Miedema, J. B. Buse, Z. Gu, Dual self-regulated delivery of insulin and glucagon by a hybrid patch. *Proc. Natl. Acad. Sci. U.S.A.* **117**, 29512–29517 (2020).

**Acknowledgments:** We thank E. Hwaun, H. Luan, and P. G. Mehta for helpful discussions. This work made use of the John O'Brien Nanofabrication Laboratory and the Core Center of Excellence in Nano Imaging at the University of Southern California. **Funding:** This work was supported by Office of Naval Research (ONR) Multidisciplinary University Research Initiative N00014-19-1-2373. H.Z. acknowledges support from the Office of Naval Research DURIP grant (N00014-21-1-2927). Q.Z., L.L., and J.S. acknowledge support from the USC Viterbi School of Engineering Graduate Fellowship. **Author contributions:** Q.Z. and H.Z. conceived the concept and designed the research. Q.Z., Y.S., J.S., and B.T. performed device fabrication and characterization. E.G., J.C., Q.Z., N.N., and R.G. performed ex vivo studies. L.L. performed finite element simulations. Q.Z., E.G., Y.S., J.C., N.N., L.L., M.G., R.G., and H.Z. analyzed the data. Q.Z. and H.Z. wrote the paper, with input from all co-authors. **Competing interests:** H.Z. and Q.Z. are inventors on two provisional patent applications filed by the University of Southern California (serial no. 63/468,959 and serial no. 63/469,024, filed 25 May 2023). The authors declare that they have no other competing interests. **Data and materials availability:** All data needed to evaluate the conclusions in the paper are present in the paper and/or the Supplementary Materials.

Submitted 23 December 2023

Accepted 29 March 2024

Published 1 May 2024

10.1126/sciadv.adn7202